Cell Reports
Physical Science

Article

Experimental correlation of anionic mass transport and lithium dendrite growth in solid-state polymer-based lithium metal batteries

Graphical abstract

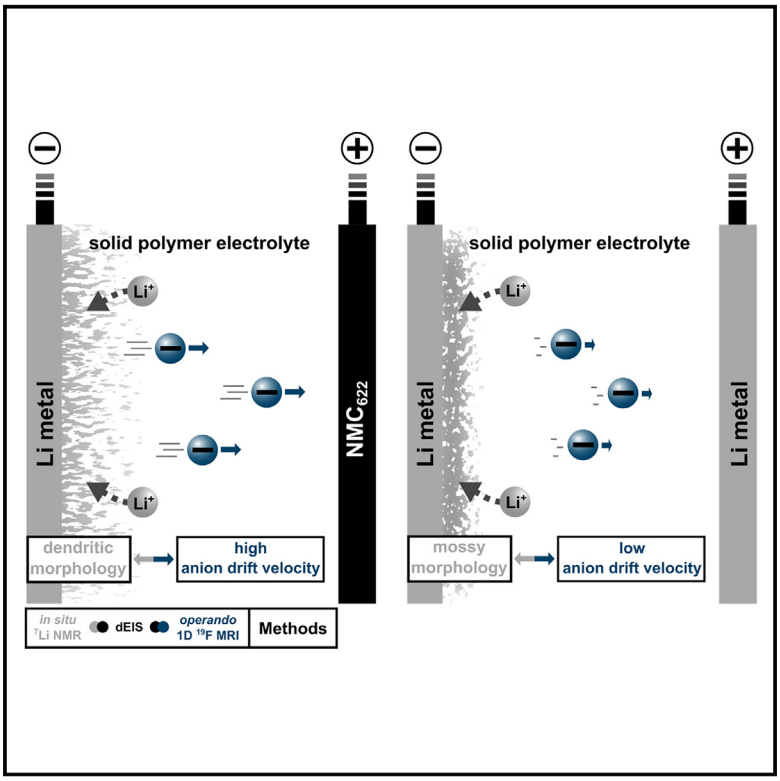

Highlights

- Experimental correlation of anionic mass transport and formation of dendritic Li
- Quantification of anion drift velocities in bulk electrolytes upon cell charging
- *Operando* method portfolio established for polymer-based alkali metal batteries
- Evidence of Chazalviel's model predictions of lithium metal deposition

Authors

Johannes H. Thienenkamp, Peter Lennartz, Martin Winter, Gunther Brunklaus

Correspondence

j.thienenkamp@fz-juelich.de (J.H.T.), g.brunklaus@fz-juelich.de (G.B.)

In brief

Thienenkamp et al. developed an *operando* method portfolio suitable for evaluation of solid-state polymer electrolytes. Fast-charge failing mechanisms of high-energy alkali metal batteries are unraveled, paving the route to tailored designs of future polymer-based alkali metal batteries.

Thienenkamp et al., 2024, Cell Reports Physical Science *5*, 102340
December 18, 2024
https://doi.org/10.1016/j.xcrp.2024.102340

CellPress

Cell Reports
Physical Science

CellPress
OPEN ACCESS

Article

Experimental correlation of anionic mass transport and lithium dendrite growth in solid-state polymer-based lithium metal batteries

Johannes H. Thienenkamp,[1,2,*] Peter Lennartz,[1] Martin Winter,[1] and Gunther Brunklaus[1,3,*]
[1]Forschungszentrum Jülich GmbH, Helmholtz-Institut Münster, IMD-4, Corrensstraße 48, 48149 Münster, NRW, Germany
[2]X (formerly Twitter): @fz_iek
[3]Lead contact
*Correspondence: j.thienenkamp@fz-juelich.de (J.H.T.), g.brunklaus@fz-juelich.de (G.B.)
https://doi.org/10.1016/j.xcrp.2024.102340

SUMMARY

Various metal deposition models have been proposed for alkali metal batteries, but the experimental accessibility of designated driving forces and characteristics of specific morphologies is still limited. A combined method portfolio comprising *operando* 1D ^{19}F MRI, *in situ* ^{7}Li NMR, and dynamic electrochemical impedance spectroscopy (EIS) experiments is presented. Experimental evidence of the relation of capacity-degrading dendritic Li metal growth and anionic mass-transport quantities beyond Sand's time in polymer-based Li metal batteries is demonstrated. Comparison of anionic mass transport and morphological changes in Li metal in Li||Li and NMC_{622}||Li cells revealed that elevated anion drift velocities within electrolytes are correlated with pronounced dendrite growth. Higher cell voltages are associated with increased anion drift velocities and hence dendrite growth, as reflected by a 2.5-fold increase in velocities in NMC_{622}||Li compared to Li||Li cells. This highlights the potential of the introduced method portfolio for experimental evaluation of polymer electrolytes and artificial coatings suitable for alkali metal batteries.

INTRODUCTION

Unfavorable morphological changes in alkali metal deposits during electrochemical operation of rechargeable alkali metal batteries, in particular lithium metal batteries (LMBs), may impose safety risks and severe capacity fading, thereby limiting the exploitation of alkali metal batteries in contemporary electric vehicle applications. Specifically, upon cell operation at faster-charge conditions (>2C), unintentional occurrence of high-surface-area (needle or dendritic shaped) metal deposits results in pronounced cell capacity fading due to the formation of so-called "dead-metal" fractions (i.e., electronically isolated alkali metal fragments) and internal short circuits.[1–4] Although several macroscopic determinants[5] with respect to alkali metal morphology changes have been identified (e.g., temperature, electrolyte composition, current density, overpotential, and stack pressure), salient mechanistic details of alkali metal nucleation and propagation are subjects of continued discussion, thus critically confining tailored developments of active materials and other cell components, comprising artificial coatings, metal pretreatments, and electrolyte constituents. Note that a sufficient reversibility of alkali metal inventory is paramount to enhance the longevity and applicability of metal-based cell designs; thus, rendering better mechanistic understanding on actual operational conditions is crucial.[6]

Despite a variety of rather complex models being proposed, aspects of alkali nucleation and propagation remain insufficiently understood. An in-depth discussion of available models, mostly focusing on Li metal deposition, can be found in recent reviews,[1,5,7–10] but briefly summarized, the models rely on key characteristics that determine alkali metal deposition: (1) "lithiophilicity" of Li metal electrodes; (2) composition and properties (e.g., structural uniformity) of solid electrolyte interphases (SEIs) present at metal surfaces; (3) surface-tension and rheological features of alkali metal electrodes, the (solid) electrolyte, and the SEI layers; (4) crystallographic properties of alkali metal (anisotropies and defects) as well as alkali metal motion at the surface; and (5) a mass-transport limitation of metal deposition. The various models contrasting initiation and propagation mechanisms indicate that the critical driving forces for obtaining distinct metal deposit morphologies are challenging to access experimentally, hence limiting further adjustment of present models. Relevant access to these quantities may be achieved by various *in situ* and *operando* methods,[11,12] where imaging techniques with sufficient temporal and spatial resolution (i.e., optical, SEM, TEM, X-ray, neutron, NMR/MRI, electron paramagnetic resonance [EPR], atomic force microscopy [AFM], etc.) constitute valuable qualitative and partly quantitative techniques to evaluate the trends of alkali metal morphology evolution and alkali metal deposit growth. Here, NMR techniques are advantageous since, particularly, Li metal morphologies can be quantitively distinguished[13–15] via characteristic changes in bulk magnetic susceptibility (BMS) associated with the different Li metal morphologies, as reflected by the observable ^{7}Li NMR

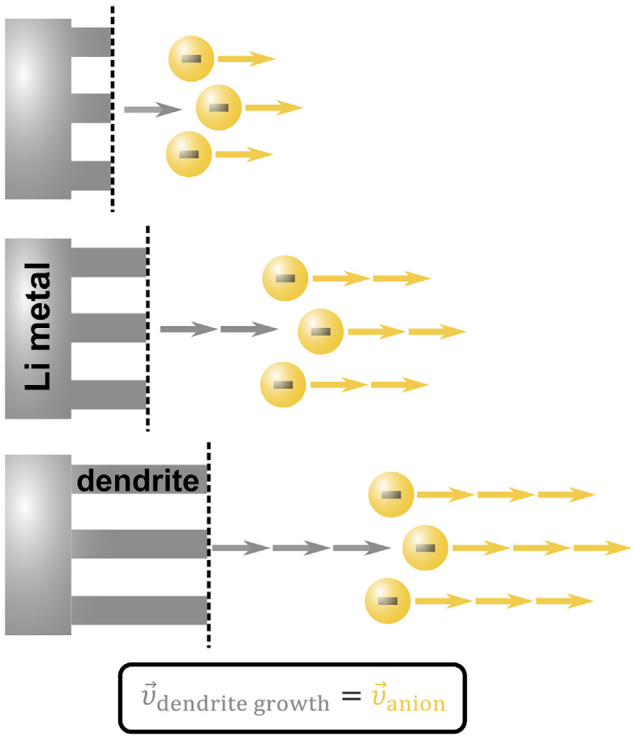

Figure 1. Chazalviel's model of dendritic lithium-metal deposition
While LMBs are charging, anions are drifting away from the lithium (Li) electrode where Li metal deposition occurs. A correlation of anionic mass transport and Li dendrite growth is suggested by Chazalviel's model. The growth velocity of dendritic Li $\vec{v}_{\text{dendrite growth}}$ is equivalent to the anion drift velocity $\vec{v}_{\text{anion}}$ in the bulk electrolyte. The nature of the electrode and electrolyte properties (including SEI) determines how fast anions are drifting within the bulk electrolyte.

chemical shifts of Li metal species. In combination with *operando* chemical-shift imaging (CSI), actual Li metal morphology changes have been successfully resolved.[16–18] In Li||Li cells operated with liquid electrolytes, Grey et al. monitored the Li deposit morphologies, ranging from mossy to dendritic-shaped, occurring at Sand's time when applying current densities above 0.51 mA cm^{-2} (constant current [CC] charging).[17] Sand's time marks the time when charge carrier depletion at electrodes' surfaces most likely occurs. The CSI experiments revealed the formation of concentration gradients of Li ions within the bulk electrolytes, where the Li ion concentration decreased in the vicinity of the lithium electrode at which lithium plating had taken place, while it increased toward the counter lithium electrode (lithium stripping). It was concluded that at conditions above a critical current density, mass-transport-limited Li metal deposition will be a dominant contributor to Li metal propagation as soon as Sand's time has been reached.

A similar conclusion was proposed by Bai and Bazant and coworkers, comparing theoretically predicted Sand's times and onset times of dendrite growth derived from optical microscopy of Li||Li cells.[19] Moreover, the onset of Li dendrite growth appeared to be correlated to sudden voltage peaks, in good agreement with Chazalviel's dendrite growth model.[20–23] In this model, anionic mass-transport limitations at Li metal electrode surfaces yields pronounced dendrite growth, model category (5), where the growth velocity of a ramified lithium front (propagation velocity) reflects an anion drift velocity within electrolytes. Anion motion is induced by the applied electric fields, and accordingly, anion drift velocities determine the nature of inhomogeneous metal deposition and Li dendrite growth (see Figure 1). It should be noted that Chazalviel's model quantifies dendrite growth at charging conditions above a critical current density, while actually, commercial batteries operated with liquid electrolytes are cycled well below such critical current densities. Also, morphological changes from mossy to dendritic-shaped Li metal deposits have already been identified for Li||Li cells at conditions below any specific critical current density and prior to reaching Sand's time, in contrast to the model's predictions.[17,23] It could be shown that even at low current densities, the Li dendrite growth followed the velocity at which the anions drifted within bulk electrolytes. Here, anion drift velocities were estimated by Ohm's law, while the dendrite growth was evaluated by optical microscopy. A correlation of these velocities seems to hold true even well below the critical current densities. Notably, a limited applicability of Chazalviel's model for cell cycling at low current densities may be attributed to oversimplified assumptions of electrode surfaces, where characteristics such as local inhomogeneities and the impact of the present SEI layers were not accounted for. Despite this, Chazalviel's model (5) was initially applied to polymer electrolytes,[22,23] in which mass-transport limitations are more prevalent compared to typical liquid electrolytes. Due to comparably low ionic conductivities of solid polymer electrolytes, the actually applied current densities in practical Li ion batteries may exceed specific critical current densities of solid polymer-based electrolytes.[24] Thus, models based on mass-transport limitations are consulted while developing polymer-based solid-state electrolytes for (Li or Na) metal batteries[25–30] and are expected to be relevant in the field of next-generation lithium batteries.[31]

To unravel detailed insights and gain better understanding of how mass-transport-induced dendrite growth governs capacity fading and operational safety of promising polymer-based Li metal batteries, the corresponding anion drift velocities can be exploited for the evaluation of polymer electrolytes, artificial coatings, and Li metal pretreatments. However, reviewing the literature, we find that these velocities have not been experimentally determined while (dis)charging LMBs yet. The ion drift velocities in binary or ternary electrolytes have been determined by e-field NMR to derive mass-transport properties such as ion mobility and transference number. For this, blocking electrodes (Pt/Pd) and voltages of up to 200 V were required, hence decoupling mass-transport properties from the respective electrode redox kinetics.[32–36] In contrast, Goward's group quantified the charge carrier transport in liquid electrolytes while polarizing graphite||Li cells, thereby including effects of concentration gradients arising from (sluggish) electrode kinetics (Li ion intercalation to graphite and lithium stripping). The concentration-dependent mass-transport properties, such as ion diffusion coefficient, transference number, and ionic conductivity, were successfully mapped in typical liquid electrolytes.[18,37–40] Compared to symmetric Li||Li cells, graphite||Li cells are advantageous in this

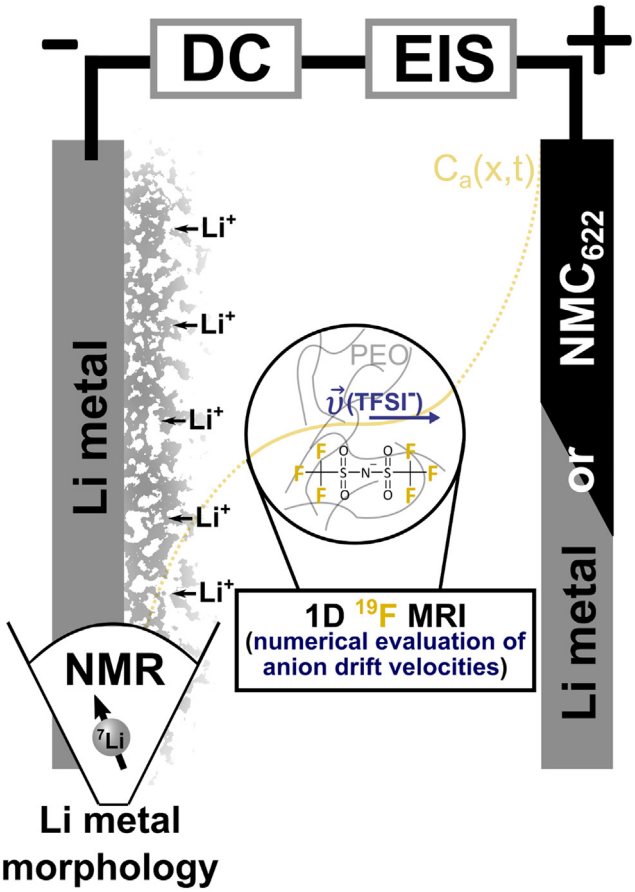

Figure 2. Schematic representation of the experimental *operando* setup

Upon charging, anion drift velocities $\vec{v}(TFSI^-)$ are obtained from numerical evaluation of corresponding anionic 1D ^{19}F MRI concentration profiles $C_a(x,t)$. At some point, anion depletion toward the negative pole (Li metal deposition: $Li^+ + e^- \rightarrow Li$) is observed. Simultaneously, the electrodes' interphase impedances are determined by dynamic EIS experiments and subsequent DRT analysis. All obtained anion drift velocities and interphase impedances are correlated to the present morphologies of Li metal deposits monitored by *in situ* ^{7}Li NMR.

respect, since the (bulk) electrolyte mass transport becomes stationary (steady-state concentration gradients) after a certain charging/polarization time (Li ion intercalation into graphite), facilitating calculations of mass transport based on rather diffusive and migrative transport equilibria.[39]

To determine electrolyte transport properties even in Li||Li cells under polarization with non-stationary mass transport, Monroe and colleagues reported a thermodynamic approach for superconcentrated electrolytes. Experimental observations of ion distributions (MRI) and overpotentials (potentiometric) while polarizing symmetric Li||Li cells agreed closely with the model's predictions.[41] Nevertheless, the work focused on the concentration-dependent transport properties reflected by charge carrier diffusion coefficients, ionic conductivities, and transference numbers. Morphological changes in Li metal deposition due to mass-transport limitations, in particular due to anionic mass transport, were out of scope. Cheng et al. examined ion depletion under galvanostatic conditions in polymer-based Li||Li cells and showed, based on *operando* stimulated Raman scattering experiments, that reduced ion concentrations, measured at least 5 μm apart from the electrode surface, led to more pronounced dendritic metal deposition, in good agreement with previous MRI results.[17,42] In addition, the authors were able to derive metal-dendrite growth velocities between 2.0 μm/min (=120 μm/h) and 5.2 μm/min (312 μm/h).

While the correlation of ion depletion and morphological changes seems to be profound, further experimental insights into correlations of dendrite growth and mass transport as proposed by Chazalviel's model are still missing, leaving main model predictions such as the claimed space-charge region and the relation of dendrite growth velocities to anion drift velocities yet to be validated. Hence, in the present work, the corresponding anion drift velocities within polymer-based Li||Li and Li||NMC_{622} cells are determined experimentally based on *operando* 1D ^{19}F MRI anion concentration profiles and numerical evaluation (Figure 2). Beyond Chazalviel's model as well as the scope of previous studies, state-of-the art cathode materials (NMC_{622}) are considered to unravel the impact of operating voltage (above 3 V) on mass transport and metal deposition. By simultaneously acquiring dynamic electrochemical impedance spectroscopy (EIS) spectra and analyzing the distribution of relaxation times (DRT), impedance changes within the Li metal electrode interphases are identified and correlated to the respective trends in anion drift velocities within the considered polymer electrolytes. Also, Li metal morphologies derived from *in situ* ^{7}Li NMR experiments are evaluated with respect to both anion drift velocities and redox processes at the electrode interfaces. While primarily exploiting ^{7}Li NMR, the proposed procedure in principle holds for other metal-based cell chemistries such as sodium metal (^{23}Na), although the stronger quadrupolar interaction could impede spectral resolution. Polyethylene oxide-based polymer electrolytes are used as a proof-of-concept model, but the introduced methodology can be similarly applied to other types of (polymer) electrolytes.[43] In summary, for the first time, anion drift velocities and Li dendrite growth are correlated experimentally in the case of polymer-based LMBs, paving the way for a more tailored design of polymer electrolytes and of artificial coatings that could allow for faster-charge applications of LMBs.

RESULTS AND DISCUSSION

Determination of anion drift velocities

In the present work, anion drift velocities are derived from *operando* 1D ^{19}F MRI concentration profiles, as briefly described below, then anion drift velocities in Li||Li and Li||NMC_{622} cells are compared and related to Li metal morphology evolution as observed by *in situ* ^{7}Li NMR. Also, DRT analysis of dynamic EIS spectra yields relevant insights into electrode interphasial processes while mass-transport limited Li metal deposition occurs.

By following the versatile framework of Chazalviel, a numerical approach is presented to derive corresponding anion drift velocities from *operando* 1D ^{19}F MRI anion profiles acquired for polarized Li||Li and Li||NMC_{622} cells. For the sake of clarity, the cell

notation utilized ("cathode"||"anode") refers to charging processes and not to the commonly used discharging processes, i.e., all cells are polarized so that Li metal is deposited on the Li metal electrodes, designating them as cathodes (reduction), and either Li or NMC_{622} counter electrodes are labeled as anodes (oxidation). A detailed description on how to derive the anion drift velocities v_a numerically at non-stationary mass-transport conditions as well as an error discussion can be found in the supplemental information (Note S1 and Note S3). Note that the following experimental input is required:

(1) *operando* 1D ^{19}F MRI anion intensity profiles of the bulk electrolyte while plating Li metal
(2) applied cell voltage while plating Li metal
(3) concentration-dependent ion diffusion coefficients obtained from pulsed-field gradient (PFG) NMR (concentration series of the electrolytes)

In brief summary and using mathematical analytic statements, 1D anionic mass transport might be derived based on a reduced Nernst-Planck approach (without convection), describing the spatial *x*- and temporal *t*-dependent anionic particle flux density $J_a(x,t)$ as a sum of diffusive $J_{diff.}(x,t)$ and migrative $J_{mig.}(x,t)$ contributions:

$$J_a(x,t) = J_{diff.}(x,t) + J_{mig.}(x,t). \quad \text{(Equation 1)}$$

Here, mass transport is governed by anionic concentration gradients $\left(\frac{\partial C_a(x,t)}{\partial x}\right)$ and experimentally applied electric field strengths $E(x,t)$) rather than the electrochemical potential gradients used in the more general framework of Newman's concentrated solution theory.[44] Ion diffusion is solely described by Fick's first law, including anion diffusion coefficients D, while ion migration results from the applied electric field strengths $E(x,t)$ and actual anion mobilities $\mu_a(x,t)$ within the electrolytes:

$$J_{diff.}(x,t) = -D\frac{dC_a(x,t)}{dx}, \quad \text{(Equation 2)}$$

$$J_{mig.}(x,t) = v_a(x,t)C_a(x,t) = -\mu_a(x,t)E(x,t)C_a(x,t). \quad \text{(Equation 3)}$$

Nernst-Planck's dilute solution theory does not take ion/ion diffusional drag interactions into account,[41] limiting the model's applicability to ideally diluted binary electrolytes. However, the most widely investigated and already commercialized polymer electrolyte PEO/LiTFSI, with reasonably high ion dissociation degrees, satisfies the prerequisites of Nernst-Planck's dilute solution theory.[36,45,46] Since Chazalviel's model is also based on dilute solution theory, we limit our interest to binary electrolytes, in agreement with previous work[22,23,47–49] focusing on PEO/LiTFSI electrolytes, to permit a derivation of anion drift velocities with a modest number of experimental parameters. The overall anionic particle flux density $J_a(x,t)$ within the bulk electrolyte can be derived from *operando* 1D ^{19}F MRI anion concentration profiles by invoking mass conservation (continuum equation):

$$\frac{d\boldsymbol{J}_a(x,t)}{dx} = -\frac{dC_a(x,t)}{dt}. \quad \text{(Equation 4)}$$

Integration of Equation 4 leads to an expression for the anionic particle flux density $\boldsymbol{J_a(x,t)}$:

$$\int \frac{dC_a(x,t)}{dt}dx = D\frac{\partial C_a(x,t)}{\partial x} + \mu_a(x,t)E(x,t)C_a(x,t). \quad \text{(Equation 5)}$$

Upon determination of the concentration-dependent (self-) diffusion coefficients of the anions from ^{19}F PFG NMR of a PEO/LiTFSI concentration series (Note S2 and Figure S3), the impact of concentration changes on the anion diffusion coefficients and anion mobilities is considered. Based on the Nernst-Einstein relation (Equation 6), the anion mobilities and diffusion coefficients can be converted into each other:

$$\mu_a(c_a) = \frac{D_a(c_a)F}{RT}. \quad \text{(Equation 6)}$$

F, R, and T represent faradaic and gas constants as well as temperature, respectively. From the indefinite integration in Equation 5 (left-hand side) arises an initial value problem, which might be solved by taking the applied cell voltage into account. The applied voltage $V_{cell}(t)$ is assumed to be composed of electric field contributions in the x direction, thereby neglecting potential gradients parallel to the electrodes' surfaces and ohmic contributions of electrolyte as well as charge-transfer resistances at the electrodes:

$$V_{cell}(t) = i\int_{cell}\rho(x,t)\,dx + \int_{cell}\boldsymbol{E}(x,t)\,dx. \quad \text{(Equation 7)}$$

i and $\rho(x,t)$ correspond to a current density and resistivity (ionic and interfacial), respectively. Here, the electric field strengths $\boldsymbol{E}(x,t)$ govern the anion drift velocities (Equation 3). Under mass-transport-limited Li metal plating conditions (galvanostatic cell polarization at limited current densities), the concentration overpotentials primarily determine the resulting cell voltages. Ion depletion eventually occurring at the lithium cathode is tackled by an increase in cell voltage and thus by an increase in electric field strength. Changes in the ionic conductivities across the diffusion layer of the electrodes and ohmic contributions of charge-transfer processes are assumed to be comparably small.[50,51] Thus, ohmic contributions to the cell voltages might be neglected, and Equation 7 can be reduced to:

$$V_{cell}(t) \approx \int_{cell}E(x,t)\,dx. \quad \text{(Equation 8)}$$

This simplification is derived from previous MRI experiments that have been modeled utilizing an irreversible thermodynamic approach. Wang et al. showed for superconcentrated electrolytes in Li||Li cells that Nernstian contributions of the cell voltage due to concentration polarization increase over time during a galvanostatic polarization experiment, while ohmic contributions resulting from the ohmic (IR) drop as well as partially from surface kinetics stayed constant or decreased over time.[41] Thus, it is to be expected that Nernstian contributions dominate the cell voltage as soon as severe concentration polarization

(=mass-transport-limited redox reaction) occurs. To thoroughly validate this simplification, however, Nernstian and ohmic contributions resulting from a diffusion layer and charge-transfer process under mass-transport-limited conditions should be elucidated by simulation and experimental means in more detail, but this is beyond the scope of the present work.

Anion drift velocities in Li||Li and Li||NMC cells

To evaluate the impact of anion drift velocities on Li metal plating, anion drift velocities in Li||Li and Li||NMC_{622} were determined. Due to uneven operating voltage windows (0–1.5 V for Li||Li and 3–4.2 V for Li||NMC_{622}), various mass-transport processes and thus different Li metal morphologies were expected. In both cases, Li metal was plated on top of the Li metal electrodes while charging the cells. The lithium plating reaction was galvanostatically driven into a mass-transport-limited condition and then held there, potentiostatically. In this way, concentration changes near the lithium electrode surface were carried in the bulk electrolyte, where anion concentration changes were observed by *operando* ^{19}F MRI (time resolution: 8 min 33 s). In the case of both cell chemistries (Li||Li and Li||NMC_{622}), steady-state anion concentration profiles in *operando* experiments could not be observed, that is, the anion mass transport was non-stationary. Under galvanostatic operation (at CC density, CC = 0.1 mA cm^{-2}), lithium plating became mass-transport limited, as indicated by the sudden cell voltage increase, after ca. 90 and 135 min for Li||Li and Li||NMC_{622} cells, respectively (Figures 3A and 3C). An additional open circuit voltage (OCV) step was required for the NMC_{622} cathodes to account for the potentially competing capacity limitation of the cathodes. However, a voltage drop of 0.5 V after the constant voltage (CV) step as well as available cathode capacity of 50% compared to the theoretically estimated cell capacities (obtained based on applied/measured currents and Faraday's law) convincingly demonstrated the presence of mass-transport limitations. Furthermore, Sand's time can be calculated from cation and anion diffusion coefficients and might be employed as a predictor when mass-transport limitations start to dominate the redox kinetics. According to Chang et al., Sand's time τ_s can be estimated by Equation 9 [17]:

$$\tau_s = \pi D \left(\frac{C_0 e}{2 i t_a} \right)^2, \qquad \text{(Equation 9)}$$

where D, C_0, e, and t_a represent the ambipolar diffusion coefficient ($m^2\ s^{-1}$), the particle concentration (L^{-1}), the elemental charge (As), and the anion transport number, respectively. Considering the obtained anion diffusion coefficient of 1.3×10^{-12} $m^2\ s^{-1}$ at 40°C (see the supplemental information), a typical anion transport number of 0.9 for PEO-based electrolytes, a particle concentration of 9.94×10^{23} L^{-1}, and an applied current density of 0.1 mA cm^{-2} results in a Sand's time of 103 min. Please note that the ambipolar diffusion coefficient was assumed to be 2.53×10^{-13} $m^2\ s^{-1}$ and was derived by first calculating the cation diffusion coefficient based on the anion diffusion coefficient and the anion transport number and, second, invoking the Nernst-Einstein relation to calculate ion mobilities. The sudden voltage changes observed at 90 and 135 min are in close proximity or after the estimated Sand's times, indicating that the Li metal deposition becomes mass-transport limited as soon as the voltage increases in both cases. Interestingly, sudden voltage changes in case of Li||NMC_{622} cells are delayed, which might be attributed to the elevated applied cell voltage compared to the Li||Li system, since the calculation of Sand's time takes only diffusive and not migrative contributions to the mass transport into account. This simplification might be sufficient for Li||Li cells with applied voltages close to 0 V, but may not be valid for more realistic cell setups like Li||NMC_{622} with applied voltages between 3.0 V and 4.2 V. Further differences between both cell configurations can be determined while comparing the derived anion drift velocities.

While mass-transport limitations deploy, an increase in anion drift velocity is observed in both cases (Figures 3B and 3D). Maximum anion drift velocities of 385 and 1,041 μm/h for Li||Li and Li||NMC_{622}, respectively, were derived. The order of magnitude of the maximum anion drift velocity derived from Li||Li cells is in good agreement with previously derived lithium-dendrite growth velocities (312 μm/h) based on stimulated Raman scattering experiments in polymer-based Li||Li cells,[42] corroborating the proposed correlation (of dendrite growth velocity and anion drift velocity) according to Chazalviel's model. Moreover, the derived anion drift velocities in Li||NMC_{622} cells are consistently larger compared to Li||Li cells, suggesting more pronounced lithium-dendrite growth in Li||NMC_{622} cells. A minus sign indicates the direction of the anion motion (against the electric field). Notably, the spatial distribution of anion drift velocities diverges over time. Chazalviel's model relates a distinct anion drift velocity to a dendrite growth velocity. Spatial divergences might be reduced by introducing a moving frame to the presented numerical approach, which scales with the divergences. In his model, Chazalviel introduced this moving frame to account for volume changes of the electrodes while stripping and plating lithium from one lithium electrode to the other. Here, the frame velocity represents the anion drift velocity, which is correlated to the dendrite growth velocity. Since only a minor fraction of Li metal is plated (about 10% of Li metal capacity), any volume changes of the electrodes are assumed to be comparably small, while a computation of moving frame velocities would require one to invoke additional minimizing methods. Thus, we limit our interpretations to the magnitude and spatial divergence over time of derived anion drift velocities while comparing the drift velocities of both cell chemistries. Note that, in this case, a more pronounced spatial divergence reflects an elevated moving frame velocity. In Figures 3B and 3D, six prominent anion drift velocities of three different profiles (belonging to the initial state, after CC, and after CV), marking the profiles' edges, are highlighted, thereby illustrating temporal and spatial evolutions of anion drift velocities. For clarity, all cell lengths are normalized to their numerically evaluated cell region (region of interest: ROI), slightly varying due to electrode size differences of Li metal and NMC_{622}. Hence, at $x_i = 0$ and at $x_i = 1$ Li metal deposition and stripping/Li ion deintercalation (NMC_{622}) occur. Comparing spatial distributions of anion drift velocities over time, an increase toward the Li metal cathode (at which lithium plating occurs) and continuous decline over space ($x_i = 0 \rightarrow 1$) is observed for both cell

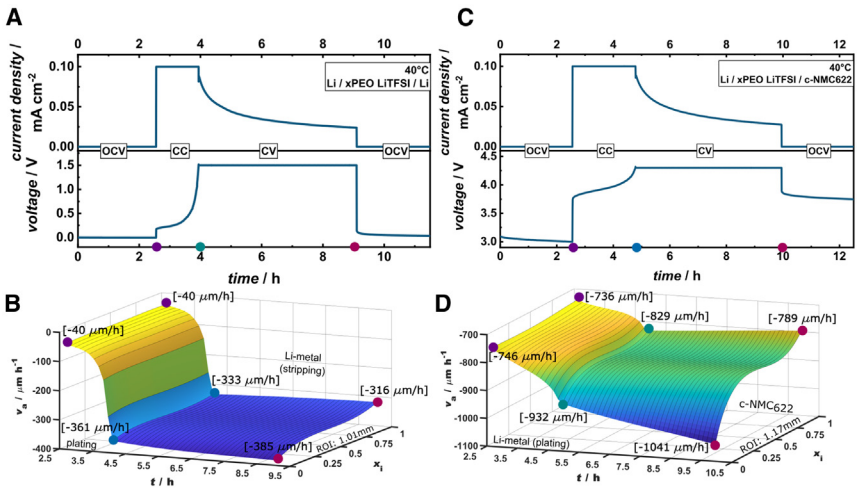

Figure 3. Anion drift velocities in Li||Li and Li||NMC cells upon charging

CC/CV polarizations and derived anion drift velocities $v_a(x,t)$ of Li||Li (A and B) and Li||NMC_{622} (C and D) cells. Negative anion drift velocities indicate anion movement against the applied electric field. In both considered cases a sudden increase in drift velocities at the end of each CC step was observed.

chemistries and at all times. The spatial differences from $x_i = 0$ to $x_i = 1$ are smaller in Li||Li cells (maximum spatial difference of ca. 18% at the end of CV) than in Li||NMC_{622} cells (maximum spatial difference of ca. 24% at the end of CV). Enhanced decelerations of anions in Li||NMC_{622} over space, likely due to smaller volume changes of NMC_{622} electrodes (anions piling up), are suggested. An increase of 6.3% (Li||Li) and 10.5% (Li||NMC_{622}) in anionic velocities at $x_i = 0$ during a CV step (after achieving the mass-transport limitation) can be noticed. During the same time, at $x_i = 1$, a comparable increase of ca. 5% (5.1% and 4.8%) was detected in both cases. All these data strongly imply pronounced lithium-dendrite growth in Li||NMC_{622} cells according to Chazalviel's model. To evaluate actual Li metal deposition morphologies, *in situ* ^{7}Li NMR spectra were recorded after cell polarizations.

Morphology of Li metal deposits

^{7}Li NMR can be utilized to evaluate morphology changes in Li metal deposits due to BMS differences of the various lithium morphologies. Due to the "Knight shift," pristine Li metal can be assigned to ^{7}Li signals at 245 ppm, and mossy and dendritic morphologies induced by Li metal deposition shift the ^{7}Li NMR signals to higher parts per million. Typically, signals arising at 260 and 270 ppm are assigned to mossy and dendritic-shaped Li metal deposits, respectively.[13,17] Please note that the parts per million shift of different morphologies is due to the orientation dependency of the BMS on the static magnetic field. The more parallel individual deposits grow with respect to the magnetic field (perpendicular to the electrode surface), the higher the respective ^{7}Li shift. Thus, the assignment of distinct morphologies to certain parts per million represents rather the general trend than the exact microstructures.[13] The exact same cells invoked for the derivation of anion drift velocities are utilized, without disassembly, to derive the impact of anion mass transport on the respective Li metal morphologies. Note that only the rf coils were changed (^{19}F → ^{7}Li). To account for BMS changes in the pristine Li metal and thus shifted ^{7}Li NMR signals attributed to cell insertion/ejection while changing rf coils, all spectra are referenced internally to the major ^{7}Li signal of pristine Li metal electrodes at 245 ppm. Slight misadjustments (±1 ppm) of the cylindrical cell axis and the external magnetic field along the z axis are thus compensated for (ideally, the unit normal vector of the electrodes' reactive sides should match the z axis).[52] *In situ* ^{7}Li NMR spectra of Li||Li and Li||NMC_{622} cells are shown in Figure 4. After cell polarization, broader signals arise next to pristine Li metal signals and cover a range of shifts, indicating the presence of high-surface-area Li metal deposits (mossy, dendritic, etc.). Note that signal intensities of both cells are normalized to the pristine Li metal signal at 245 ppm. Experimentally obtained signals are deconvoluted into three different signals, thereby obtaining fitted ^{7}Li NMR line shapes that match the experimental data within R^2 = 99.8%. Line-shape deconvolution is carried out without chemical shift constraints to distinguish Li metal morphology differences in both considered cell chemistries. Shifts of the deconvoluted signals are rounded to the nearest whole values. Further, we limit our interpretation to the BMS shifts (center of gravity) of deconvoluted signals, since the counter lithium electrode in Li||Li cells and skin-depth effects prevent quantification and comparison of signal intensities (at least in the case of pristine Li metal signals).[53] Nonetheless, a comparison of BMS shifts (purple deconvoluted signal) reveals that the Li metal deposits are more of dendritic shape in Li||NMC_{622} compared to Li||Li cells, since a shift toward higher ppm (268 ppm) can be observed in the case of Li||NMC_{622}, while more mossy morphologies at 263 ppm are identified in Li||Li cells. Although the optimization method invoked (Levenberg-Marquardt) ran without shift constraints (upon deconvolution), two signals at 245 and 250 ppm, respectively, are present in both cells. While the signals at 245 ppm obviously belong to bulk Li metal, the signals at 250 ppm might reflect dense Li metal deposits arising from the nucleation process during the CC polarization (until Sand's time has been reached) or can be assigned to asymmetric contributions of the bulk Li metal signals due to long-range BMS effects of mossy and dendritic-shaped Li metal deposits at even higher ppm affecting the symmetry of the bulk lithium signals, as previously reported by Bhattacharyya et al.[54] Here, the authors required an additional signal upon deconvolution to account for the mentioned asymmetry of the bulk Li metal signal. The additional signal is shifted a few parts per million higher than the pristine Li metal signal, in good agreement with our results. Thus, morphological differences in both cells and a correlation between anionic mass transport and dendrite growth can be reasonably assumed. To further explore the proposed relationship of anion drift velocities and lithium dendrite

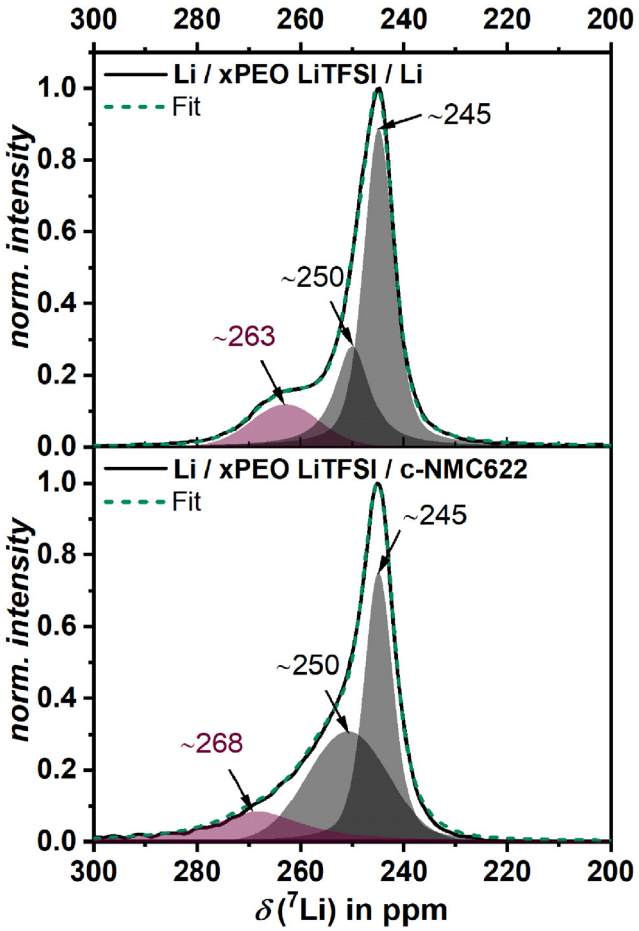

Figure 4. Morphology of lithium metal deposits Li||Li and Li||NMC after charging

In situ ^{7}Li NMR spectra of Li||Li and Li||NMC$_{622}$ cells measured immediately after polarization and the last OCV step. Three morphologies of Li metal deposits are accounted for. The deconvolution succeeded without chemical shift constraints to identify morphology differences. In both cases, deconvoluted line shapes fit within R^2 = 99.8%. More dendritic Li metal deposition is observed in Li||NMC$_{622}$ compared to Li||Li cells.

growth rates, a combined approach of *operando* ^{7}Li CSI (spatially resolved observation of dendrite growth) and operando ^{19}F MRI anion profiling may provide detailed insights but is beyond the scope of the present work. Nevertheless, all the required experimental preparations are currently in progress and will be reported in due time.

Lithium interphase evolution—dynamic EIS

The profile's edges obtained by frequency-encoded 1D MRI are affected by B_0 inhomogeneities and any eddy currents (due to rf pulses and z gradients) induced by the electrodes.[55] Thus, we limit our presented numerical approach to anionic concentration profiles within the bulk electrolytes (ROI). Processes occurring directly at the Li metal interfaces or within the diffusion layer are still obscured; therefore, the existence of Chazalviel's proposed space-charge region[20] is not experimentally verified. To gain more insight into the electrode kinetics and mass transport processes in the vicinity of the electrode surfaces, dynamic EIS spectra were recorded simultaneous with *operando* ^{19}F MRI profiling. DRT analysis of *operando* EIS data was exploited to identify electrochemical processes based on characteristic relaxation time constants τ.[56–58] Mass-transport-related changes within electrolytes observed by MRI were complemented by electrode interphase processes (e.g., charge transfer, double layer, or diffusion layer effects), so that time constants in the range of $-4 < \log(\tau) < 0$ were explicitly considered. Note that the time-consuming low-frequency EIS experiments (<1 Hz, $\log(\tau) > 0$) are neglected to reduce acquisition times of individual EIS spectra, as this is required for *operando* experiments, in which time-invariant state-of-charge conditions upon EIS acquisition are necessary. Figures 5B and 5E display normalized DRT functions $h(\tau)$ during polarization (CC/CV) and normalized resistances (Figures 5C and 5F) resulting from the integrated DRT functions. Normalized resistances reflect intersections of RC semicircles with the Z' axis in Nyquist plots. Similar to the derived anion drift velocities, the normalized DRT functions $h\,(\log(\tau))$ increase at the end of each CC step in Li||Li and Li||NMC$_{622}$ cells and increase further during the CV step, while all peaks at $\log(\tau) \approx -3$ shift toward lower time constants. A shift in time constants might be attributed to morphological changes in Li metal deposition and is currently being investigated. A continuous growth of interphase resistances monitored during the CV steps and a sudden decrease of interphase resistances after the CV step (Figures 5C and 5F) are noted in both cell chemistries, indicating dynamic interphase processes (e.g., varying size of diffusion layers). Also, resulting resistances of interphase processes increase upon CV, eventually approaching constant slopes, but no steady-state condition is reached, indicating continuous changes in all the underlying interphasial processes. Both increase and continuous changes over time are consistent with transient evolution of anion drift velocities during CC/CV polarization, illustrating that non-stationary electrode kinetics cause non-stationary anionic mass transport, which is observable by MRI. The non-stationary changes in the corresponding anion drift velocities during CV polarization likely reflect contributions from both moving boundaries (i.e., volume changes of the electrode) and ongoing changes in interphasial processes. Furthermore, resistances are usually associated with ohmic contributions, which have been neglected when considering concentration overpotentials as part of resulting voltages (Equation 8). Interphase resistances typically include interphasial processes from both electrodes, so that, accounting for both electrodes in Li||Li cells contributing equally to the actual interphase resistances, the interphase resistance of a singular electrode in Li||Li cells is half of the total. Even under these terms, the measured interphasial resistances in Li||Li cells are still higher than in the case of Li||NMC$_{622}$ cells (15 kohm cm^{-2} vs. 10 kohm cm^{-2} at the end of the CV steps). Thus, the observed trend in anion drift velocities and hence Li dendrite growth ($v_a(x,t)_{\mathrm{Li||NMC_{622}}} > v_a(x,t)_{\mathrm{Li||Li}}$) is not affected by higher ohmic resistances. Note that capacitive impedances also increase during CC/CV steps.

Methodological restrictions and broader applicability

The calculated anion drift velocities are derived from a dilute solution approach. To extend the applicability to a variety of

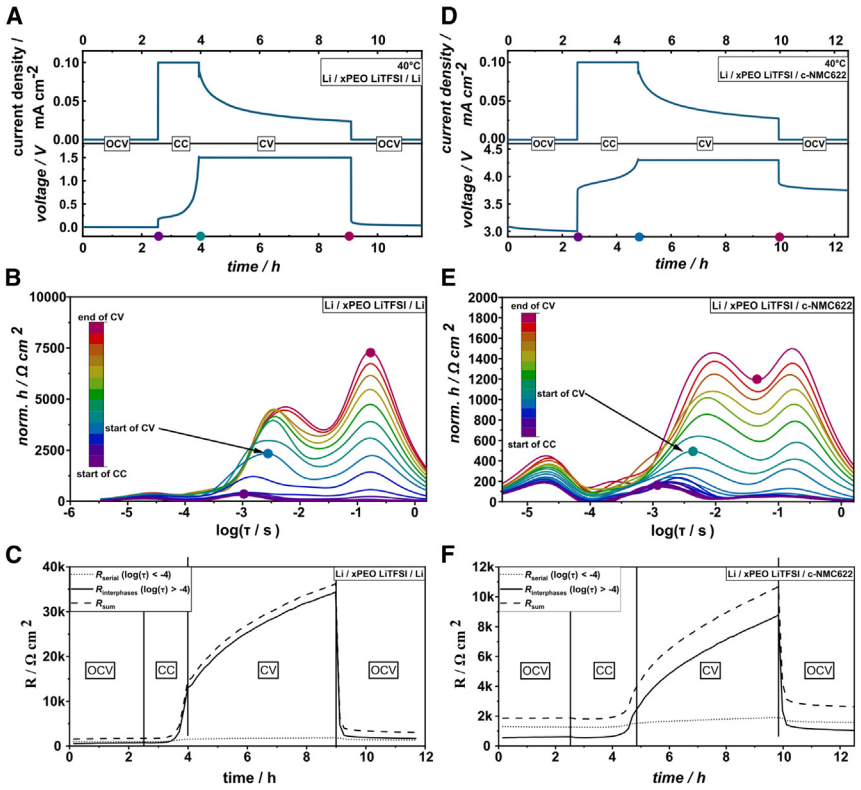

Figure 5. Lithium interphase evolution via dynamic EIS

CC/CV polarization and DRT plots of Li||Li (A and B) and Li||NMC_{622} cells (D and E). (C) and (F) represent the integrated areas of (B) and (E) vs. time. The color code in (B) and (E) corresponds to selected *operando* EIS experiments equally separated in time (step size of CV equals five times CC step size). Relaxation times in the range of $-4 < \log(\tau) < 0$ are attributed to processes at electrode interphases.

polymer electrolyte systems, concentrated solution theory might be invoked. To this end, Chazalviel's model needs to be derived from concentrated solution theory to demonstrate that the correlation of anion drift velocities and lithium dendrite growth is still valid. Equation 10 might be used to describe anionic mass transport in concentrated binary electrolyte systems composed of anions, cations, and solvent (without convection):

$$J_a(x,t) = -\frac{n_a \mathfrak{D}}{nRT}\frac{c_T}{c_0} c \frac{d\phi_e(x,t)}{dx} + \frac{i t_a^0}{z_a F}, \qquad \text{(Equation 10)}$$

where $n = n_c + n_a$ describes the total number of cations and anions produced by the dissociation of one molecule of electrolyte and ϕ_e, t_a^0, and i represent the electrochemical potential of the electrolyte, the anionic transference number with respect to the solvent velocity, and the current density, respectively. Please note that Maxwell-Stefan diffusion needs to be considered rather than Fickian diffusion. For further details, please see Chapter 12 ("Concentrated Solutions") of Newman's and Balsara's 4th edition of *Electrochemical Systems*.[50]

So far, morphological changes in Li metal have been described by various models covering distinct cycling conditions of LMBs, but often suffered from lack of experimental accessibility. Herein, a combined approach of *operando* 1D ^{19}F MRI anion concentration profiling, *in situ* ^{7}Li NMR, and dynamic EIS is introduced to experimentally examine anionic mass transport and inhomogeneous dendritic Li metal deposition, since the well-known model derived by Chazalviel correlates anionic drift velocities with growth velocities of a ramified lithium deposition front under mass-transport-limited conditions. The model is often invoked for the development of next-generation solid-state polymer-based electrolytes for LMBs, in which mass-transport limitations occur due to limited ionic conductivities of solid polymer electrolytes. Based on our presented numerical approach, anion drift velocities within the bulk electrolyte are derived from *operando* 1D ^{19}F MRI anion profiles in Li||Li and Li||NMC_{622} cells while charging the batteries and accounting for non-stationary mass transport. Under mass-transport-limited conditions (that is, at fast-charge conditions or higher current densities), a sudden increase in anion drift velocities up to several hundreds of micrometers per hour is observed in both cell setups. The magnitude of derived anion drift velocities is in good agreement with previously observed dendrite growth velocities under mass-transport-limited conditions, supporting the proposed correlation between anionic mass transport and dendrite growth velocity by Chazalviel's model. Also, the respective anion drift velocities in Li||NMC_{622} cells exceed the anion drift velocities in Li||Li cells, which is most likely attributable to the higher operating cell voltage applied in the case of NMC-type cathodes (3.0–4.2 V instead of 0–1.5 V). Due to the introduction of an NMC-type cathode, electric field contributions might become more dominant with respect to the ionic mass transport, which might additionally be reflected by the observed delayed Sand's time in the case of in Li||NMC_{622} cells. Beyond that, spatial distributions of anion drift velocities are observed in both cases, while the spatial differences are more pronounced in Li||NMC_{622} cells. Subsequent *in situ* ^{7}Li NMR spectra revealed Li metal deposits of more dendritic shape in the case of Li||NMC_{622} compared to Li||Li cells. The elevated anion drift velocities and more pronounced dendrite growth rates are in agreement with Chazalviel's model. In addition, DRT analysis of dynamic EIS spectra showed a reversible, but non-stationary, increase in interphasial impedances (charge transfer, double and diffusion layer effects) under mass-transport-limited conditions, highlighting that metal deposition kinetics affect long-range (anion) mass-transport processes within bulk electrolytes (as observed by MRI). In both cases, a shift in relaxation times (DRT) of interphasial processes toward higher values indicates morphological changes in the

metal deposition once mass-transport limitation conditions are established. In summary, the invoked experimental setup and numerical approach afford experimental accessibility to Chazalviel's dendrite growth model and rates of metal deposition, revealing mechanistic insights into morphological changes in (Li, Na, etc.) metal deposits, depending on the actual conditions of cell operation. The anion drift velocity might be used as a performance indicator for polymer-based solid-state LMBs to evaluate reversibility of lithium inventory and thus capacity retention of LMBs. Adjusting anion drift velocities in the bulk electrolyte by optimizing anion and cation mass transport within the diffusion layer of Li metal electrodes, e.g., by incorporating single-ion conductors as artificial SEIs or by facilitating more homogeneous electrode kinetics via optimized SEI formation (additives) or more advanced pretreatments of the Li metal electrode, will permit a more tailored design of polymer electrolytes and coatings. This method portfolio gives access to these decisive anion drift velocities for the first time and paves the way to faster charge applications of polymer-based (Li, Na, etc.) metal batteries. It is noted that incorporation of *operando* (^{7}Li) CSI to the protocol in principle further extends the portfolio of accessible observables, mitigating current challenges of metal-based cell chemistries.

EXPERIMENTAL PROCEDURES

NMR setup for *operando* and *in situ* experiments

Simultaneous utilization of *operando* anion concentration MRI profiling and *operando* EIS of solid-state Li||Li and Li||NMC_{622} cells with cross-linked PEO electrolyte was performed. All the NMR spectra were recorded on a BRUKER Avance III 4.7 T spectrometer using a modified BRUKER Diff50 probe and a 10 mm ^{19}F insert for 1D ^{19}F MRI profiling, a 10 mm ^{7}Li insert for ^{7}Li NMR spectra, and a 5 mm ^{7}Li/^{19}F insert for PFG experiments. The temperature was controlled with BRUKER BCU20 temperature units and kept at 40°C for all the experiments. Since a TC1 thermocouple of the commercial BRUKER probe was changed to a DC/AC-current lamella connector, the corresponding sample temperatures were calibrated based on data from an external thermocouple (±0.02°C). Similar to previous works,[39,59] a home-built cylindrical polyether ether ketone (PEEK) model cell housing was manufactured with a PEEK 3D printer (Apium P220).

Operando 1D ^{19}F anion concentration MRI profiling

Operando 1D ^{19}F anion concentration MRI profiles were acquired with a frequency-encoded and modified BRUKER "diffprof" pulse program capable of constant pulse and receiver phases. To enclose the full cell stack, the field of view (FOV) was adjusted to 4 mm. A bandwidth of 100 kHz was selected to decrease the sampling time of *k* vectors and avoid profile deformation at higher bandwidths, resulting in maximum gradient strengths of 62.4 G cm^{-1}. One hundred twenty-eight gradient steps (derived from the complex time domain, bandwidth, and group delay) were applied, yielding an echo acquisition time of 1.48 ms and a nominal spatial resolution of 31.25 μm. With an echo delay of 160 μs, a recycle delay of 4 s, and 128 scan repetitions, a single MRI profile was recorded within 8 min and 33 s. Note that the rf (radio frequency) field strength was set to 18,181 Hz, corresponding to a $\pi/2$ pulse length of 13.25 μs. All the spectra were evaluated in a BRUKER Topspin 3.5pl7 (magnitude mode and Fourier transformation) and further processed with an in-house custom-made MATLAB script.

In situ ^{7}Li NMR spectra

Static 1D ^{7}Li spectra were recorded with a custom-made electrolyte suppression Hahn echo pulse program. To facilitate data evaluation (deconvolution), magnetization at around 0 ppm was averaged by presaturation (200 repetitions of a "sinc"-shaped pulse) prior to applying a common Hahn echo pulse program with short echo delays of 20 ms. The transmitter frequency was changed from 0 ppm (presaturation) to 255 ppm (Hahn echo) during one repetition, while the rf power changed from a selective pulse (=714 Hz) to a more broadband pulse (=18,181 Hz). One thousand twenty-four repetitions and a recycle delay of 0.4 ms resulted in an experimental time of 8 min and 15 s. All spectra were internally referenced to Li metal (set to 245 ppm[13]). The ^{7}Li spectra were acquired 1 h after obtaining the last 1D ^{19}F MRI profile. Fast Fourier transformation and phase correction were done in a BRUKER TopSpin 3.5pl7, whereas spectral deconvolution was done with dmfit software.[60] Note that no baseline correction was required.

Dynamic EIS and cell polarization

All electrochemical experiments were carried out with a Zahner Zennium Pro galvanostat with an integrated EIS module and proprietary Thales software. *Operando* EIS test procedures consisted of four consecutive "direct current" (DC) steps while acquiring EIS spectra: (1) an OCV step for 2.5 h (thermal equilibration), (2) a CC step, (3) a CV step for 5 h, and (4) an OCV step for 2.5 h. A current density (CC step) of 0.1 mA cm^{-2} and a CV step of 1.5 V for Li||Li or 4.3 V for Li||NMC_{622} cells were applied. The CC steps ended when the voltage of the set CV was reached (1.5 or 4.3 V), whereas CV steps were limited only by time (5 h). The applied current densities (0.1 mA cm^{-2}) and CVs were set sufficiently high to induce electrolyte mass-transport limitation of electrode reactions, in particular for Li metal plating. This condition was noted based on a sudden voltage increase during the CC steps. In the case of Li||Li cells, this sudden voltage increase could be directly related to mass-transport limitations, whereas for Li||NMC_{622} cells, a comparison of OCVs before and after CC/CV steps was additionally required to exclude capacity limitation from cathodes. Applying CVs of equal magnitude (compared to the last measured voltages at the end of each CC step) maintained a mass-transport limit for Li metal plating over time. At the end of each ^{19}F MRI anion profile acquisition, impedance spectra were recorded so that the experiments ended simultaneously. During the CC and OCV steps, the corresponding AC amplitude of the galvanostatic impedance experiments was set to one-third of the applied DC density, thus achieving reasonable impedance spectra without interfering with the state of charge. An AC amplitude of 50 mV was utilized for potentiostatic impedance experiments during the CV step. All impedance spectra were recorded in a frequency range from 1 Hz to 100 kHz, resulting in an experimental time for each EIS spectrum of 1 min and 9 s (six steps per decade and four repetitions). Experimental data were exported and analyzed by home-made Python scripts to derive normalized distribution functions of relaxation times (DRT analysis) as described elsewhere.[61,62] Using a regularization parameter of 0.5 as well as 92 time constants, Kramers-Kronig residuals[56] of less than 3% were achieved. Relaxation times in the range from 1 s to 0.1 ms were assigned to electrode interphase processes, so that changes in the normalized distribution functions reflect changes within electrode interphases due to electrode reactions.[56]

PFG NMR

To determine ^{19}F self-diffusion coefficients, a concentration series of LiTFSI in cross-linked PEO was prepared and measured using a double-tuned 5 mm ^{7}Li/^{19}F insert and a stimulated echo pulse sequence. KF (3 M in H_2O) was utilized for external calibration. The rf power was set to 21,276 Hz, the maximum gradient strength to 2,946 G/cm, the diffusion time Δ to 60 ms, the gradient pulse length δ to 1 ms, and the recycle delay to 6 s. Each of the 16 gradient steps was averaged from 16 scans. Self-diffusion coefficients of the fluorine species (anions) were derived from a stimulated echo sequence (BRUKER "diffSte") after fitting the overall attenuated signal amplitudes (integration) to the Stejskal-Tanner equation that describes the case of ideal isotropic diffusion.

Materials and cell assembly

The introduced combination of *operando* techniques was applied to two cell systems. System 1 was a symmetric Li||Li solid-state battery, whereas system 2 represented a Li||NMC_{622} solid-state battery. Note that the actual operating voltage denoted the major difference between the two cells. All cells were assembled within an MBraun glovebox (with values of <0.1 ppm O_2, <0.1 ppm H_2O, and <0.1 ppm CO_2).

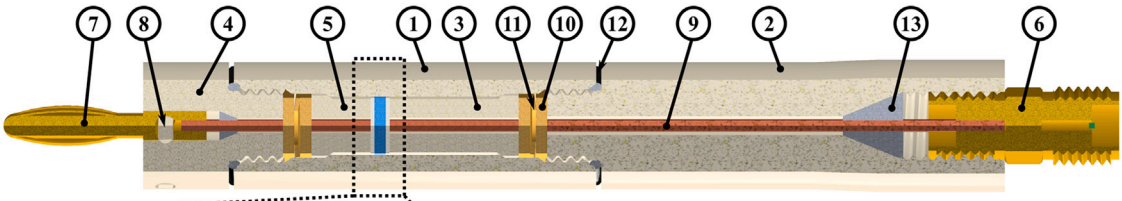

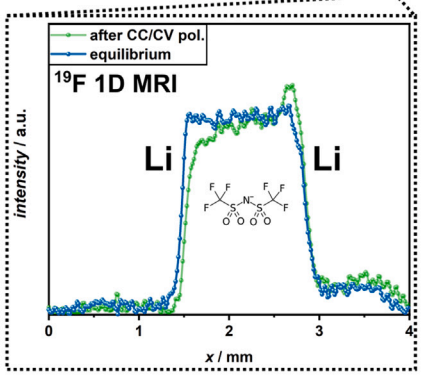

no.	part	material	amount
1	sleeve	PEEK	1
2	outer right plug	PEEK	1
3	inner right plug	PEEK	1
4	outer left plug	PEEK	1
5	inner left plug	PEEK	1
6	SMA F/F adapter	gold coated	1
7	lamella adapter	gold coated	1
8	fixing pin	PEEK	1
9	1 mm Ø copper wire	copper	4
10	1 mm contact plates (6mm Ø)	beryllium copper	4
11	disc springs (0.15 mm stroke distance)	beryllium copper	2
12	O-rings	FPM	2
13	2-component glue	silicon-based	2

Figure 6. Electrolyte preparation and cell assembly

Schematic representation of an MRI cell (top). Its outer diameter is 10 mm, and the inner diameter (measurement volume) amounts to 6 mm. Within the measurement volume, the cell stack (e.g., Li|electrolyte|Li) is located. For the sake of clarity, electrolyte and electrodes are colored blue and gray. The inset at the left shows an exemplary ^{19}F 1D anionic MRI intensity profile.

Electrode preparation

Composite NMC_{622} (c-NMC622) cathodes were prepared by a slurry-based approach incorporating an interpenetrating polymer-based electrolyte system[63] to afford good contacts of active material and polymers. The electrodes consisted of 60 wt % NMC_{622} (BASF), 10 wt % carbon black (Super P, Targray), and 30 wt % electrolyte comprising LiTFSI (3M, predried) and a PEO (M_w 400 kDa, Sigma-Aldrich) to PEGdMA (polyethylene glycol dimethacrylate, M_w 750 Da, Sigma-Aldrich, predried) mass ratio of 1:0.45 as well as a PEGdMA to AIBN (azobisisobutyronitrile, Sigma-Aldrich) mass ratio of 1:10, resulting in a molar EO:Li ratio of 10:1. They were produced by first dissolving PEO and PEGdMA in acetonitrile (400 wt % of total electrode mass) followed by the addition of NMC622, carbon black, LITFSI, and AIBN. The mixture was homogenized using a VMA-Getzmann CV3-plus Dispermate (2,000 rpm for 2 h at 15°C). Then, the slurry was cast on aluminum foils using doctor blading prior to transferring the electrode sheets to a vacuum oven (Binder vacuum oven). Acetonitrile was evaporated at reduced pressure (10^{-3} mbar at 25°C for 12 h) followed by polymerizing the PEGdMA at 80°C under N_2 flux for 2 h and subsequently drying for 12 h at 80 °C at reduced pressure (10^{-3} mbar). Average cathode active mass (CAM) loading was set to 8.0 mg cm^{-2}, sufficiently high to avoid capacity limitations during *operando* measurements. Before the cell assembly, all the electrodes were dried under high vacuum (10^{-7} mbar) and transferred to a glovebox. As-received 300 μm Honjo Li metal (stored in a glovebox, <0.1 ppm O_2, <0.1 ppm H_2O, and <0.1 ppm CO_2) was used as the Li metal electrode for both systems.

Electrolyte preparation and cell assembly

For solid-state LMBs, a cross-linked PEO-based polymer electrolyte was manufactured as described previously.[64] Electrolyte preparation was conducted in a dry room atmosphere (dew point < −65°C). PEO (0.605 g; 5 Mio Da, Sigma-Aldrich) was mortared with 0.395 g LiTFSI (EO:Li = 10:1, purchased from 3M) and 0.05 g benzophenone initiator (TCI Germany). The mixture was formed into a ball, vacuumed sealed, and heated to 100°C for 24 h to ensure homogeneity. Regarding the concentration series, only the amount of LiTFSI was changed. The homogenized balls were hot pressed to 100-μm-thin membranes at 100°C and 10 bar for 5 min and subsequently at 100°C and 100 bar for 5 min. Five minutes of UV curing (Hönle UVA 100 cube) completed the membrane preparation.

For the MRI cells, 65 mg of the homogenized balls was filled in a dummy cell consisting of a cell sleeve and two dummy plugs (without current collectors) to enclose a volume of 1.5 mm in height and 6 mm in diameter (volume of cell sleeve; see Figure 6), preventing lithium dendrites from short circuiting the cell and facilitating acquisition of distortionless MRI intensity profiles of bulk electrolytes. The cells were vacuum sealed (pouch foil) and heated to 100°C for another 1.5 h to create cylindrical (6 mm diameter) polymer electrolyte pellets of 1.5 mm height (=active volume). Afterward, the dummy cells were cooled to room temperature (=21°C) and carefully removed from the cells to cross-link the polymer electrolyte based on 5 min UV curing (Hönle UVA 100 cube). The cell housings with the polymer electrolyte pellets were then dried at reduced pressure (10^{-7} mbar) and transferred to a glovebox for cell assembly. Six-millimeter-diameter electrodes were added to the cells (Li||Li or Li||NMC_{622}) and closed by preassembled plugs. Added electrodes were lightly pressed into the soft polymer electrolyte to ensure interfacial contact.[65] The internal pressure was released by heating the cell up to the operating temperature of 40°C as parts of the polymer-based electrolytes were squeezed past the electrodes (visible as small intensities next to the main anionic MRI profiles, see Figure 6). To counteract volume changes of the polymer electrolyte during heating, two beryllium copper disk springs with stroke distance of 0.15 mm each surrounded by two 1-mm-thick contact plates ensuring electrical contact were included. In this way, a cylindrical measurement volume of a minimum of 6 mm in diameter times 1.5 mm in height was available. Due to the disk springs, a measurement volume of a maximum of 6 mm in diameter and 1.8 mm in height was guaranteed. The electrodes' thickness of 300 μm (Li metal) or 80 μm (NMC_{622}) as well as the malleability of the polymer electrolyte at 40°C has to be considered to estimate the measurement volume of the MRI experiments (see ROIs).

RESOURCE AVAILABILITY

Lead contact

Requests for further information and materials, datasets, scripts, and more should be directed to and will be fulfilled by the lead contact, Gunther Brunklaus (g.brunklaus@fz-juelich.de).

Materials availability

Composite cathodes as well as MRI cell components generated in this study are available from the lead contact on request.

Data and code availability

The datasets and MATLAB script generated during this study can be downloaded here: Zenodo: https://doi.org/10.5281/zenodo.14103250.

The DRT script is available here: Zenodo: https://doi.org/10.5281/zenodo.14067949.

Technical drawings of the MRI cell are available on request.

ACKNOWLEDGMENTS

Generous funding from the German Federal Ministry of Education and Research (BMBF) via the grants "For-Analytik" (13XP0445) and FB2-POLY (13XP0429A) is acknowledged. The authors thank Melanie M. Mitchell for reviewing the manuscript and offering her valuable suggestions for its improvement.

AUTHOR CONTRIBUTIONS

Conceptualization, J.H.T. and G.B.; formal analysis, investigation, and methodology, J.H.T.; DRT examination, P.L. and J.H.T.; visualization and writing – original draft, J.H.T.; writing – review & editing, J.H.T., P.L., G.B., and M.W.; supervision, G.B. and M.W.

DECLARATION OF INTERESTS

The authors declare no competing interests.

SUPPLEMENTAL INFORMATION

Supplemental information can be found online at https://doi.org/10.1016/j.xcrp.2024.102340.

Received: July 26, 2024
Revised: October 21, 2024
Accepted: November 21, 2024
Published: December 18, 2024

REFERENCES

1. Horstmann, B., Shi, J., Amine, R., Werres, M., He, X., Jia, H., Hausen, F., Cekic-Laskovic, I., Wiemers-Meyer, S., Lopez, J., et al. (2021). Strategies towards enabling lithium metal in batteries: interphases and electrodes. Energy Environ. Sci. *14*, 5289–5314. https://doi.org/10.1039/D1EE00767J.
2. Zhang, R., Shen, X., Zhang, Y.-T., Zhong, X.-L., Ju, H.-T., Huang, T.-X., Chen, X., Zhang, J.-D., and Huang, J.-Q. (2022). Dead lithium formation in lithium metal batteries: A phase field model. J. Energy Chem. *71*, 29–35. https://doi.org/10.1016/j.jechem.2021.12.020.
3. Aktekin, B., Riegger, L.M., Otto, S.-K., Fuchs, T., Henss, A., and Janek, J. (2023). SEI growth on Lithium metal anodes in solid-state batteries quantified with coulometric titration time analysis. Nat. Commun. *14*, 6946. https://doi.org/10.1038/s41467-023-42512-y.
4. Wood, K.N., Kazyak, E., Chadwick, A.F., Chen, K.-H., Zhang, J.-G., Thornton, K., and Dasgupta, N.P. (2016). Dendrites and Pits: Untangling the Complex Behavior of Lithium Metal Anodes through Operando Video Microscopy. ACS Cent. Sci. *2*, 790–801. https://doi.org/10.1021/acscentsci.6b00260.
5. Li, Z., Huang, J., Yann Liaw, B., Metzler, V., and Zhang, J. (2014). A review of lithium deposition in lithium-ion and lithium metal secondary batteries. J. Power Sources *254*, 168–182. https://doi.org/10.1016/j.jpowsour.2013.12.099.
6. Brunklaus, G., Lennartz, P., and Winter, M. (2024). Metal electrodes for next-generation rechargeable batteries. Nat. Rev. Electr. Eng. *1*, 79–92. https://doi.org/10.1038/s44287-023-00006-5.
7. Chen, X.-R., Zhao, B.-C., Yan, C., and Zhang, Q. (2021). Review on Li Deposition in Working Batteries: From Nucleation to Early Growth. Adv. Mater. *33*, 2004128. https://doi.org/10.1002/adma.202004128.
8. Hou, J., Yang, M., Sun, B., and Wang, G. (2022). Improvement Strategies toward Stable Lithium-Metal Anodes for High-Energy Batteries. Batter. Supercaps *5*, 231. https://doi.org/10.1002/batt.202200231.
9. Ramasubramanian, B., Reddy, M.V., Zaghib, K., Armand, M., and Ramakrishna, S. (2021). Growth Mechanism of Micro/Nano Metal Dendrites and Cumulative Strategies for Countering Its Impacts in Metal Ion Batteries: A Review. Nanomaterials *11*, 2476. https://doi.org/10.3390/nano11102476.
10. Zou, P., Sui, Y., Zhan, H., Wang, C., Xin, H.L., Cheng, H.-M., Kang, F., and Yang, C. (2021). Polymorph Evolution Mechanisms and Regulation Strategies of Lithium Metal Anode under Multiphysical Fields. Chem. Rev. *121*, 5986–6056. https://doi.org/10.1021/acs.chemrev.0c01100.
11. Foroozan, T., Sharifi-Asl, S., and Shahbazian-Yassar, R. (2020). Mechanistic understanding of Li dendrites growth by in- situ/operando imaging techniques. J. Power Sources *461*, 228135–228158. https://doi.org/10.1016/j.jpowsour.2020.228135.
12. Strauss, F., Kitsche, D., Ma, Y., Teo, J.H., Goonetilleke, D., Janek, J., Bianchini, M., and Brezesinski, T. (2021). Operando Characterization Techniques for All-Solid-State Lithium-Ion Batteries. Adv. Energy and Sustain. Res. *2*, 2100004. https://doi.org/10.1002/aesr.202100004.
13. Chang, H.J., Trease, N.M., Ilott, A.J., Zeng, D., Du, L.-S., Jerschow, A., and Grey, C.P. (2015). Investigating Li Microstructure Formation on Li Anodes for Lithium Batteries by in Situ ^{6}Li/^{7}Li NMR and SEM. J. Phys. Chem. C *119*, 16443–16451. https://doi.org/10.1021/acs.jpcc.5b03396.
14. Hsieh, Y.-C., Leißing, M., Nowak, S., Hwang, B.-J., Winter, M., and Brunklaus, G. (2020). Quantification of Dead Lithium via In Situ Nuclear Magnetic Resonance Spectroscopy. Cell Reports Physical Science *1*, 100139–100154. https://doi.org/10.1016/j.xcrp.2020.100139.
15. Gunnarsdóttir, A.B., Amanchukwu, C.V., Menkin, S., and Grey, C.P. (2020). Noninvasive In Situ NMR Study of "Dead Lithium" Formation and Lithium Corrosion in Full-Cell Lithium Metal Batteries. J. Am. Chem. Soc. *142*, 20814. https://doi.org/10.1021/jacs.0c10258.
16. Chandrashekar, S., Trease, N.M., Chang, H.J., Du, L.-S., Grey, C.P., and Jerschow, A. (2012). 7Li MRI of Li batteries reveals location of microstructural lithium. Nat. Mater. *11*, 311–315. https://doi.org/10.1038/NMAT3246.
17. Chang, H.J., Ilott, A.J., Trease, N.M., Mohammadi, M., Jerschow, A., and Grey, C.P. (2015). Correlating Microstructural Lithium Metal Growth with Electrolyte Salt Depletion in Lithium Batteries Using ^{7}Li MRI. J. Am. Chem. Soc. *137*, 15209–15216. https://doi.org/10.1021/jacs.5b09385.
18. Krachkovskiy, S., Trudeau, M.L., and Zaghib, K. (2020). Application of Magnetic Resonance Techniques to the In Situ Characterization of Li-Ion Batteries: A Review. Materials *13*, 1694. https://doi.org/10.3390/ma13071694.
19. Bai, P., Li, J., Brushett, F.R., and Bazant, M.Z. (2016). Transition of lithium growth mechanisms in liquid electrolytes. Energy Environ. Sci. *9*, 3221–3229. https://doi.org/10.1039/C6EE01674J.
20. Chazalviel, J. (1990). Electrochemical aspects of the generation of ramified metallic electrodeposits. Phys. Rev. *42*, 7355–7367. https://doi.org/10.1103/PhysRevA.42.7355.
21. Fleury, V., Chazalviel, J., and Rosso, M. (1992). Theory and experimental evidence of electroconvection around electrochemical deposits. Phys. Rev. Lett. *68*, 2492–2495. https://doi.org/10.1103/PhysRevLett.68.2492.
22. Brissot, C., Rosso, M., Chazalviel, J.N., Baudry, P., and Lascaud, S. (1998). In situ study of dendritic growth inlithium/PEO-salt/lithium cells. Electrochim. Acta *43*, 1569–1574. https://doi.org/10.1016/S0013-4686(97)10055-X.

23. Brissot, C., Rosso, M., Chazalviel, J.N., and Lascaud, S. (1999). Dendritic growth mechanisms in lithium/polymer cells. J. Power Sources *81–82*, 925–929. https://doi.org/10.1016/S0378-7753(98)00242-0.

24. Song, Z., Chen, F., Martinez-Ibañez, M., Feng, W., Forsyth, M., Zhou, Z., Armand, M., and Zhang, H. (2023). A reflection on polymer electrolytes for solid-state lithium metal batteries. Nat. Commun. *14*, 4884. https://doi.org/10.1038/s41467-023-40609-y.

25. Stolz, L., Hochstädt, S., Röser, S., Hansen, M.R., Winter, M., and Kasnatscheew, J. (2022). Single-Ion *versus* Dual-Ion Conducting Electrolytes: The Relevance of Concentration Polarization in Solid-State Batteries. ACS Appl. Mater. Interfaces *14*, 11559–11566. https://doi.org/10.1021/acsami.2c00084.

26. Calderón, C.A., Vizintin, A., Bobnar, J., Barraco, D.E., Leiva, E.P., Visintin, A., Fantini, S., Fischer, F., and Dominko, R. (2020). Lithium Metal Protection by a Cross-Linked Polymer Ionic Liquid and Its Application in Lithium Battery. ACS Appl. Energy Mater. *3*, 2020–2027. https://doi.org/10.1021/acsaem.9b02309.

27. Borzutzki, K., Nair, J.R., Winter, M., and Brunklaus, G. (2022). Does Cell Polarization Matter in Single-Ion Conducting Electrolytes? ACS Appl. Mater. Interfaces *14*, 5211–5222. https://doi.org/10.1021/acsami.1c19097.

28. Chen, G., Niu, C., Liao, X., Chen, Y., Shang, W., Du, J., and Chen, Y. (2020). Boron-containing single-ion conducting polymer electrolyte for dendrite-free lithium metal batteries. Solid State Ionics *349*, 115309–115316. https://doi.org/10.1016/j.ssi.2020.115309.

29. Tian, L., Kim, J.-W., and Kim, D.-W. (2024). Solid hybrid electrolytes based on conductive oxides and polymer electrolytes for all-solid-lithium batteries. Mater. Chem. Front. *8*, 455–484. https://doi.org/10.1039/D3QM00736G.

30. Szczęsna-Chrzan, A., Marczewski, M., Syzdek, J., Kochaniec, M.K., Smoliński, M., and Marcinek, M. (2022). Lithium polymer electrolytes for novel batteries application: the review perspective. Appl. Phys. A *129*, 1–20. https://doi.org/10.1007/s00339-022-06269-3.

31. Liu, J., Bao, Z., Cui, Y., Dufek, E.J., Goodenough, J.B., Khalifah, P., Li, Q., Liaw, B.Y., Liu, P., Manthiram, A., et al. (2019). Pathways for practical high-energy long-cycling lithium metal batteries. Nat. Energy *4*, 180–186. https://doi.org/10.1038/s41560-019-0338-x.

32. Fang, C., Halat, D.M., Mistry, A., Reimer, J.A., Balsara, N.P., and Wang, R. (2023). Quantifying selective solvent transport under an electric field in mixed-solvent electrolytes. Chem. Sci. *14*, 5332–5339. https://doi.org/10.1039/D3SC01158E.

33. Fang, Y., Yushmanov, P.V., and Furó, I. (2020). Improved accuracy and precision in electrophoretic NMR experiments. Current control and sample cell design. J. Magn. Reson. *318*, 106796. https://doi.org/10.1016/j.jmr.2020.106796.

34. Halat, D.M., Fang, C., Hickson, D., Mistry, A., Reimer, J.A., Balsara, N.P., and Wang, R. (2022). Electric-Field-Induced Spatially Dynamic Heterogeneity of Solvent Motion and Cation Transference in Electrolytes. Phys. Rev. Lett. *128*, 198002. https://doi.org/10.1103/PhysRevLett.128.198002.

35. Lorenz, M., Kilchert, F., Nürnberg, P., Schammer, M., Latz, A., Horstmann, B., and Schönhoff, M. (2022). Local Volume Conservation in Concentrated Electrolytes Is Governing Charge Transport in Electric Fields. J. Phys. Chem. Lett. *13*, 8761–8767. https://doi.org/10.1021/acs.jpclett.2c02398.

36. Rosenwinkel, M.P., and Schönhoff, M. (2019). Lithium Transference Numbers in PEO/LiTFSA Electrolytes Determined by Electrophoretic NMR. J. Electrochem. Soc. *166*, A1977–A1983. https://doi.org/10.1149/2.0831910jes.

37. Bazak, J.D., Allen, J.P., Krachkovskiy, S.A., and Goward, G.R. (2020). Mapping of Lithium-Ion Battery Electrolyte Transport Properties and Limiting Currents with In Situ MRI. J. Electrochem. Soc. *167*, 140518. https://doi.org/10.1149/1945-7111/abc0c9.

38. Sethurajan, A.K., Foster, J.M., Richardson, G., Krachkovskiy, S.A., Bazak, J.D., Goward, G.R., and Protas, B. (2019). Incorporating Dendrite Growth into Continuum Models of Electrolytes: Insights from NMR Measurements and Inverse Modeling. J. Electrochem. Soc. *166*, A1591–A1602. https://doi.org/10.1149/2.0921908jes.

39. Krachkovskiy, S.A., Bazak, J.D., Werhun, P., Balcom, B.J., Halalay, I.C., and Goward, G.R. (2016). Visualization of Steady-State Ionic Concentration Profiles Formed in Electrolytes during Li-Ion Battery Operation and Determination of Mass-Transport Properties by in Situ Magnetic Resonance Imaging. J. Am. Chem. Soc. *138*, 7992–7999. https://doi.org/10.1021/jacs.6b04226.

40. Sethurajan, A.K., Krachkovskiy, S.A., Halalay, I.C., Goward, G.R., and Protas, B. (2015). Accurate Characterization of Ion Transport Properties in Binary Symmetric Electrolytes Using In Situ NMR Imaging and Inverse Modeling. J. Phys. Chem. B *119*, 12238–12248. https://doi.org/10.1021/acs.jpcb.5b04300.

41. Wang, A.A., Gunnarsdóttir, A.B., Fawdon, J., Pasta, M., Grey, C.P., and Monroe, C.W. (2021). Potentiometric MRI of a Superconcentrated Lithium Electrolyte: Testing the Irreversible Thermodynamics Approach. ACS Energy Lett. *6*, 3086–3095. https://doi.org/10.1021/acsenergylett.1c01213.

42. Cheng, Q., Wei, L., Liu, Z., Ni, N., Sang, Z., Zhu, B., Xu, W., Chen, M., Miao, Y., Chen, L.-Q., et al. (2018). Operando and three-dimensional visualization of anion depletion and lithium growth by stimulated Raman scattering microscopy. Nat. Commun. *9*, 2942–2952. https://doi.org/10.1038/s41467-018-05289-z.

43. Lennartz, P., Paren, B.A., Herzog-Arbeitman, A., Chen, X.C., Johnson, J.A., Winter, M., Shao-Horn, Y., and Brunklaus, G. (2023). Practical considerations for enabling Li|polymer electrolyte batteries. Joule *7*, 1471–1495. https://doi.org/10.1016/j.joule.2023.06.006.

44. Newman, J., and Balsara, N.P. (2021). Electrochemical Systems (John: Wiley & Sons), pp. 249–266.

45. Chintapalli, M., Timachova, K., Olson, K.R., Mecham, S.J., Devaux, D., DeSimone, J.M., and Balsara, N.P. (2016). Relationship between Conductivity, Ion Diffusion, and Transference Number in Perfluoropolyether Electrolytes. Macromolecules *49*, 3508–3515. https://doi.org/10.1021/acs.macromol.6b00412.

46. Mistry, A., Yu, Z., Peters, B.L., Fang, C., Wang, R., Curtiss, L.A., Balsara, N.P., Cheng, L., and Srinivasan, V. (2022). Toward Bottom-Up Understanding of Transport in Concentrated Battery Electrolytes. ACS Cent. Sci. *8*, 880–890. https://doi.org/10.1021/acscentsci.2c00348.

47. Monroe, C., and Newman, J. (2003). Dendrite Growth in Lithium/Polymer Systems. J. Electrochem. Soc. *150*, A1377. https://doi.org/10.1149/1.1606686.

48. Rosso, M., Brissot, C., Teyssot, A., Dollé, M., Sannier, L., Tarascon, J.-M., Bouchet, R., and Lascaud, S. (2006). Dendrite short-circuit and fuse effect on Li/polymer/Li cells. Electrochim. Acta *51*, 5334–5340. https://doi.org/10.1016/j.electacta.2006.02.004.

49. Rosso, M., Gobron, T., Brissot, C., Chazalviel, J.N., and Lascaud, S. (2001). Onset of dendritic growth in lithium/polymer cells. J. Power Sources *97–98*, 804–806. https://doi.org/10.1016/S0378-7753(01)00734-0.

50. Newman, J., and Balsara, N.P. (2021). Electrochemical Systems (John, Wiley & Sons), pp. 424–434.

51. Bard, A.J., and Faulkner, L.,R. (2000). Electrochemical Methods: Fundamentals and Applications (John Wiley & Sons), pp. 106–107.

52. Ilott, A.J., Chandrashekar, S., Klöckner, A., Chang, H.J., Trease, N.M., Grey, C.P., Greengard, L., and Jerschow, A. (2014). Visualizing skin effects in conductors with MRI: 7Li MRI experiments and calculations. J. Magn. Reson. *245*, 143–149. https://doi.org/10.1016/j.jmr.2014.06.013.

53. Küpers, V., Kolek, M., Bieker, P., Winter, M., and Brunklaus, G. (2019). In situ ^{7}Li-NMR analysis of lithium metal surface deposits with varying electrolyte compositions and concentrations. Phys. Chem. Chem. Phys. *21*, 26084–26094. https://doi.org/10.1039/C9CP05334D.

54. Bhattacharyya, R., Key, B., Chen, H., Best, A.S., Hollenkamp, A.F., and Grey, C.P. (2010). In situ NMR observation of the formation of metallic

lithium microstructures in lithium batteries. Nat. Mater. *9*, 504–510. https://doi.org/10.1038/NMAT2764.

55. Ilott, A.J., Mohammadi, M., Chang, H.J., Grey, C.P., and Jerschow, A. (2016). Real-time 3D imaging of microstructure growth in battery cells using indirect MRI. Proc. Natl. Acad. Sci. USA *113*, 10779–10784. https://doi.org/10.1073/pnas.1607903113.

56. Danzer, M.A. (2019). Generalized Distribution of Relaxation Times Analysis for the Characterization of Impedance Spectra. Batteries *5*, 53–69. https://doi.org/10.3390/batteries5030053.

57. Hahn, M., Schindler, S., Triebs, L.-C., and Danzer, M.A. (2019). Optimized Process Parameters for a Reproducible Distribution of Relaxation Times Analysis of Electrochemical Systems. Batteries *5*, 43–64. https://doi.org/10.3390/batteries5020043.

58. Krewer, U., Röder, F., Harinath, E., Braatz, R.D., Bedürftig, B., and Findeisen, R. (2018). Review—Dynamic Models of Li-Ion Batteries for Diagnosis and Operation: A Review and Perspective. J. Electrochem. Soc. *165*, A3656–A3673. https://doi.org/10.1149/2.1061814jes.

59. Klamor, S., Zick, K., Oerther, T., Schappacher, F.M., Winter, M., and Brunklaus, G. (2015). 7Li in situ 1D NMR imaging of a lithium ion battery. Phys. Chem. Chem. Phys. *17*, 4458–4465. https://doi.org/10.1039/C4CP05021E.

60. Massiot, D., Fayon, F., Capron, M., King, I., Le Calvé, S., Alonso, B., Durand, J.-O., Bujoli, B., Gan, Z., and Hoatson, G. (2002). Modelling one- and two-dimensional solid-state NMR spectra. Magn. Reson. Chem. *40*, 70–76. https://doi.org/10.1002/mrc.984.

61. Lennartz, P., Borzutzki, K., Winter, M., and Brunklaus, G. (2021). Viscoelastic polyborosiloxanes as artificial solid electrolyte interphase on lithium metal anodes. Electrochim. Acta *388*, 138526–138538. https://doi.org/10.1016/j.electacta.2021.138526.

62. Frenck, L., Lennartz, P., Parkinson, D.Y., Winter, M., Balsara, N.P., and Brunklaus, G. (2022). Failure Mechanisms at the Interfaces between Lithium Metal Electrodes and a Single-Ion Conducting Polymer Gel Electrolyte. ACS Appl. Mater. Interfaces *14*, 53893–53903. https://doi.org/10.1021/acsami.2c16869.

63. Homann, G., Stolz, L., Neuhaus, K., Winter, M., and Kasnatscheew, J. (2020). Effective Optimization of High Voltage Solid-State Lithium Batteries by Using Poly(ethylene oxide)-Based Polymer Electrolyte with Semi-Interpenetrating Network. Adv. Funct. Mater. *30*, 2006289–2006297. https://doi.org/10.1002/adfm.202006289.

64. Chen, Y.-H., Hsieh, Y.-C., Liu, K.L., Wichmann, L., Thienenkamp, J.H., Choudhary, A., Bedrov, D., Winter, M., and Brunklaus, G. (2022). Green Polymer Electrolytes Based on Polycaprolactones for Solid-State High-Voltage Lithium Metal Batteries. Macromol. Rapid Commun. *43*, 2200335–2200349. https://doi.org/10.1002/marc.202200335.

65. Roering, P., Overhoff, G.M., Liu, K.L., Winter, M., and Brunklaus, G. (2024). External Pressure in Polymer-Based Lithium Metal Batteries: An Often-Neglected Criterion When Evaluating Cycling Performance? ACS Appl. Mater. Interfaces *16*, 21932–21942. https://doi.org/10.1021/acsami.4c02095.